molecular pharmaceutics

Article

Enhanced Reactive Oxygen Species Levels by Active Benzothiazole Complex mediated Fenton Reaction for Highly Effective Anti-tumor Therapy

Chaoqun You, Hongshuai Wu, Zhiguo Gao, Fanghui Chen,
Like Ning, Yu Zhang, yixin Dong, Baiwang Sun, and Fei Wang

Mol. Pharmaceutics, **Just Accepted Manuscript** • DOI: 10.1021/acs.molpharmaceut.9b00819 • Publication Date (Web): 29 Oct 2019

Just Accepted

is published by the American Chemical Society. 1155 Sixteenth Street N.W., Washington, DC 20036

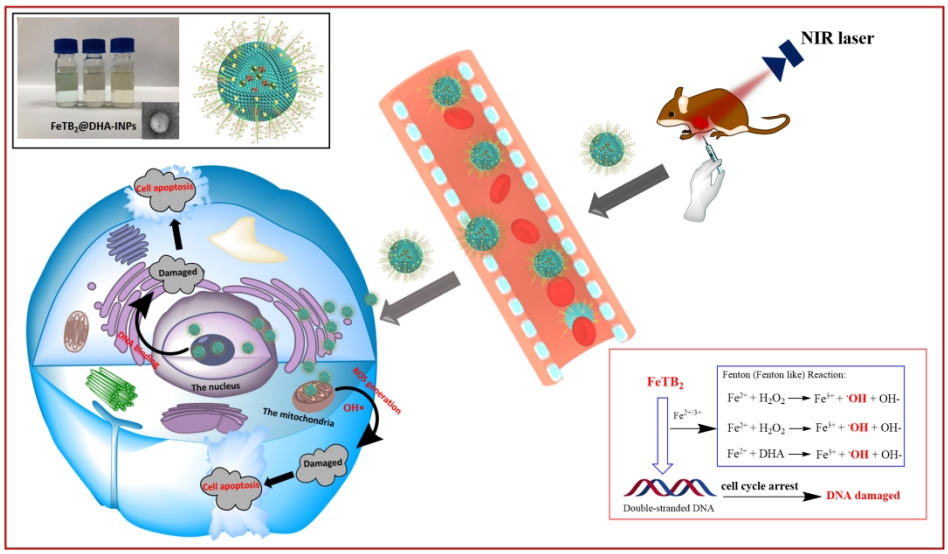

An active benzothiazole complex-filled Fenton reaction activable FeTB2@DHA−INPs polymer grafted liposomes to display ROS mediated chemodynamic therapy (CDT).

744x515mm (72 x 72 DPI)

Enhanced Reactive Oxygen Species Levels by Active Benzothiazole Complex Mediated Fenton Reaction for Highly Effective Anti-Tumor Therapy

Chaoqun You [1], Hongshuai Wu [2], Zhiguo Gao [2], Fanghui Chen [2], Like Ning [1], Yu Zhang [1], Yixin Dong [1], Baiwang Sun [2,*], Fei Wang [1,*]

1 College of Chemical Engineering, Nanjing Forestry University; Jiangsu Key Lab for the Chemistry and Utilization of Agro-Forest Biomass, Nanjing 210037, PR China Fax: +86 25 85427649, Tel: +86 25 85427649, E-mail address: hgwf@njfu.edu.cn

2 School of Chemistry and Chemical Engineering, Southeast University, Nanjing 210089, PR China. Fax: +86 25 52090614, Tel: +86 25 52090614, E-mail address: chmsunbw@seu.edu.cn

Abstract

Breaking the threshold of intracellular reactive oxygen species (ROS) levels can cause non-specific oxidative damage to proteins, and lead to the Fenton reaction-mediated exogenous ROS production to be a new promising anticancer strategy. However, the problems including the inefficient transport of metal catalysts and insufficient endogenous hydrogen peroxide (H_2O_2) content in cells still need to be improved. In this study, functional nanosystem encapsulated with benzothiazole complexes ($FeTB_2$) and the photosensitizer indocyanine green (ICG) was designed for highly effective antitumor therapy. The surface of the nanocarriers was modified with dihydroartemisinin (DHA)-grafted polyglutamic acid. The induced hyperthermia enables the lipid-polymer shell to depolymerize, releasing $FeTB_2$. The released $FeTB_2$ could kill tumor cells in two different ways by inhibiting DNA replication and catalyzing H_2O_2 to produce active •OH. Moreover, the conjugated DHA could increase the amount of peroxides in tumor cells and significantly enhance ROS yield. This work has provided solid evidence that the present nanosystem enables significant effect on

tumor killing through the combined inhibition of DNA replication and ROS mediated oxidative damage by regulation of tumor microenvironment, providing a ROS-mediated high efficiency antitumor strategy.

Keywords: Reactive oxygen species, Dihydroartemisinin, Benzothiazole derivatives, Fenton reaction, Synergistic therapy

1. Introduction

Reactive oxygen species (ROS) show important biological functions in organisms. ROS includes superoxide anion radicals (O_2•-), singlet oxygen ($^1O_2$), hydrogen peroxide (H_2O_2) and hydroxyl radicals (•OH).[1,2] Different levels of ROS lead to different biological effects in cells. When intracellular ROS levels are low, it acts as an important 2nd messenger in cell proliferation and homeostasis by reversibly oxidizing the mercapto group of proteins to modify their structure and function. For example, ROS promotes the expression of Cyclin D1, activates MAPK (mitogen-activated protein kinase), ERK (extracellular signal regulated kinase), JNK (c-Jun N-terminal kinase), all of which promote cell growth and survival.[3] However, when intracellular ROS levels are high, the tumor suppressor PTEN (phosphatase and tensin homolog deleted on chromosome ten) is reversibly inactivated,[4] leading to the non-specific oxidative damage of cellular DNA, proteins and lipids, subsequently promoting apoptosis, necrosis, and cancer.[5]

Studies have shown that in the presence of Fe^{2+}, H_2O_2 can be converted to •OH by the Fenton reaction. Since •OH has a short half-life (10^{-9} s) and high reactivity, it does not diffuse from the production site, but rapidly oxidizes surrounding biomolecules. This new regulatory form of cell death that relies on Fe^{2+} and ROS is called Ferroptosis.[6-8] Moreover, this treatment by regulating ROS levels in tumor cells, representing a new anticancer strategy.

When designing the Fenton reaction system, ROS generation is maximized under the premise of good biocompatibility and lack of toxic side effects, so as to obtain a high tumor killing efficiency. In order to obtain maximum catalytic efficiency, transporting metals in the form of ions can effectively improve the load efficiency. Nie

et al reported iron oxide nanoparticles loaded with linoleic acid hydroperoxide (LAHP).[9] The surface of the nanoparticles dissociated Fe^{2+} and reacted with LAHP to generate large amount of ROS following their internalization into cancer cells. Shi et al used endogenous H_2O_2 in tumor cells, which when combined with Fe^{2+} and FeS_2, respectively, produced large amount of ROS, leading to high anticancer efficiency.[10,11]

Benzothiazole contains a benzene ring embedded five-membered heterocyclic ring, that has been widely used for the research and development of anti-tumor drugs.[12,13] Benzothiazole derivatives exert anti-tumor effects through kinase inhibition, apoptosis induction, and action on DNA.[14-17] El-Falouji et al[18] reported a series of benzothiazole complexes in which a benzothiazole derivative and a trivalent metal ion were coordinated. These complexes exhibited strong binding ability to calf thymus DNA and showed anti-angiogenic effect.

Artemisinin is a sesquiterpene lactone containing a peroxide group which is isolated from the plant Artemisia, artesunate, artemether and dihydroartemisinin (DHA) which are derivatives of artemisinin. Among them, DHA molecules have higher water solubility, are more easily absorbed, display high efficiency, and low toxicity.[19] Recent studies found that,[20-22] DHA acts on the mitochondria-dependent apoptotic pathway to inhibit NF-κB activation, thereby promoting tumor cell apoptosis and inhibiting cell cycle progression. Moreover, DHA directly inhibits tumor cells through Fe^{2+} catalysis. Finally, DHA acts on the fibrinolytic system uPA and inhibits VEGF-induced angiogenesis to inhibit tumor invasion and metastasis.

At present work, we designed and prepared a functional nanocarrier that was internally encapsulated with functional benzothiazole complexes ($FeTB_2$) and the photosensitizer indocyanine green (ICG). The surface of the nanocarrier was modified with DHA-grafted polyglutamic acid. The hyperthermia induced by the photothermal conversion performance of ICG under NIR irradiation caused the lipid-polymer shell to depolymerize, releasing $FeTB_2$. The released $FeTB_2$ could not only directly killed tumor cells by inducing DNA arrest, but the Fe^{3+} catalyzes H_2O_2 production in the tumor microenvironment to produce large levels of active •OH, which further leads to oxidative damage. In addition, the conjugated DHA further complements the

intracellular peroxides and affectively enhances the transition of Fenton reactions. The present nanosystems effectively kill tumor cells by inducing DNA arrest and ROS mediated oxidative damage, and providing a ROS-mediated high-efficiency antitumor strategy.

2. Materials and Methods

2.1 Materials

2-Mercaptobenzothiazole, Dihydroartemisinin, Cholesterol, Lecithin, Indocyanine green (ICG) were purchased from Sigma-Aldrich Chemical Company (St. Louis, MO, USA). Poly-L-glutamic acid, HOOC-PEG_{2000}-DSPE was purchased from Polymtek Biomaterial Co., Ltd. (Shenzhen, China). All the dye kits were obtained from Beyotime Biotechnology Co., Ltd (Shanghai, China). All the other chemical reagents were obtained from Sinopharm Chemical Reagent Co., Ltd (Beijing, China).

2.2 Synthesized Procedure

2.2.1 Synthesis and characterization of Fe(III) -2- thioacetate benzothiazole

The 2-Thioacetic acid benzothiazole was prepared according to the method in literature.[23] Briefly, 2-Mercaptobenzothiazole (0.90 g, 3.0 mmol), Chloroacetic acid (1.15 g, 6.0 mmol) were dissolved in aqueous methanol (20 mL) in the presence of KOH (0.1 mol) and the mixture was refluxed for 4 h. Then the mixture solution was filtered and washed with diluted hydrochloric acid (3×5 mL), extracted with aqueous ethanol (3×10 mL). The details of the synthetic procedure was shown in Figure S1. The desired intermediate products were obtained after being concentrated and dried under reduced pressure. The product was recovered as a yellowish white solid (0.65 g, 73%). ^{1}H NMR (600 MHz, DMSO-d_6): d (ppm) 11.12 (d, 1H), 7.48 (d, 1H), 7.36 (d, 1H), 7.25-7.30 (d, 2H), 1.73 (m, 2H); ESI-MS (m/z): 226.1312 $[M + H]^+$.

Next, 2-Thioacetic acid benzothiazole (1.0 mmol, 0.224 g), triethylamine (1.0 mmol, 0.102 g) was dissolved in ethanol (20 mL) and the mixture was stirred for 20 min at 25 ^oC. The $FeCl_3.6H_2O$ dissolved in ethanol (0.5 mmol, 20 mL) and then added slowly to the prepared solution. The brown precipitate appeared immediately after mixing the two components and then stirred overnight at room temperature. The

product was obtained after filtration, purification and drying under vacuum. The desired product as a brown solid (0.79 g, 55%). Yield: 55%; IR (KBr, n/cm^{-1}): 3342, 1730, 1703, 1621, 1556, 1026, 686 and 513 cm^{-1}; ^{1}H NMR (600 MHz, DMSO-d$_6$): d (ppm) 7.73 (d, 1H), 7.41 (d, 1H), 7.25–7.30 (d, 2H), 2.52 (m, 2H); ESI-MS (m/z): 504.8122 [M + H]$^{+}$.

2.2.2 Synthesis and characterization of PGlu-SS-DHA lipid-polymer chains (DHA-PGlu–PEG$_{2000}$–DSPE)

The dihydroartemisinin modified lipid-polymer chains was synthesized through poly-L-glutamic acid with three steps as described in Figure S2. The intermediate products (PGlu-PEG$_{2000}$-DSPE and DHA-PIP) were synthesized according our previous study.[24] Next, PGlu-PEG$_{2000}$-DSPE (0.50 g, 0.12 mmol) and DHA-PIP (0.13 g, 0.36 mmol) were dissolved in DMF (15 mL) and then the mixture was stirred for 24 h at room temperature in the presence of DMAP (0.02 g, 0.15 mmol). Then the white precipitate formed as the reaction progressed and then transferred, redissolved in deionized water (5 mL). The desired product was freeze-dried from deionized water with a solid powder form after dialysis (MWCO 4000Da, water was replaced every 6 h). ^{1}H NMR (600 MHz, DMSO-d$_6$): d (ppm) 5.34 (d, 10H), 4.05 (d, 10H), 4.01 (d, 10H), 3.36 (d, ~10H), 3.05–2.51 (b, ~4000H), 1.99–0.75 (m, ~400H).

2.3 Self-Assembly and Characterizations

The designed functional nanosystems (FeTB$_2$@DHA-INPs) were prepared according the published literatures.[25-27] Briefly, DHA-PGlu$_{10}$–PEG$_{2000}$–DSPE (3.0 mg), cholesterol (2.0 mg) and lecithin (20.0 mg) were dissolved in chloroform (40 mL) and a thin film was formed after solvent evaporation. To this film was added 15 mL of FeTB$_2$ aqueous solution (0.2 mg mL^{-1}), 5 mL of ICG aqueous solution (0.4 mg mL^{-1}) and then ultrasonic vibrated for 10 min. The prepared nanosystem suspension was then centrifuged at 2500 rpm for 20 min, the supernatant was then collected, filtrated and lyophilized.

2.4 Photothermal Effects and Drug Release

To evaluate the photothermal effects of the prepared nanosystem, different concentrations of FeTB$_2$@DHA-INPs suspension (10, 20, and 40 μg mL^{-1}) were investigated after irradiation with a near-infrared laser (808 nm, 1.5 W cm^{-1}) for 5 min

and the temperature variation was detected with an infrared (IR) thermal camera (every 30 s). Before the evaluation, the photostability of $FeTB_2$@DHA-INPs suspension were tested.

The in vitro drug release of $FeTB_2$@DHA-INPs was performed as the published literatures described.[28-30] Briefly, a predesigned amount of the suspensions (3 mL, 1.5 mg mL^{-1}) in dialysis bag (MW, 10 000) was immersed in PBS (15 mL, pH = 7.4, 6.8 and 5.5) and then irradiated by an 808 nm near-infrared laser (1.5 W cm^{-1}, 5 min). A certain volume (2 mL) of the dissolution medium was taken out during each designed release period and an equal volume of fresh medium was added instead. The amount of released $FeTB_2$ in the dialysate was calculated by ICP-AES and each group was tested in triplicate.

2.5 Uptake and Co-localization into Mitochondria.

A549 and MCF-7 cells were cultured in 6-well plates (9.0×10^4 cells $well^{-1}$) and cultured for 24 h, then a certain concentration of ICG (50.0 μg mL^{-1}) in $FeTB_2$@DHA-INPs suspension (3 mL) was added into the medium. The cells were cleaned and stained with DAPI and further observed by CLSM after been incubated for 1.5, and 3.0 h. In addition, the fluorescence intensity of the intracellular ICG was calculated by flow cytometer. Next, the cells were treated with $FeTB_2$@DHA-INPs as above and then incubated for 3 h, stained with Lysotracker Green (lysosome staining, green color) to evaluate the uptake of lysosomes.

2.6 Reactive Oxygen Species (ROS) Generation

A549 and MCF-7 cells were seeded in 6-well plates at a density of 3.0×10^5 cells per well and cultured for 24 h. The cells were then treated with different concentrations (10, 20, and 30 μg mL^{-1}) of nanoparticles for 3 h. Then the cells were treated with DCF-DA (10 μM) for 30 min and then analysis by flow cytometry. Similarly, different incubation time (0.5 h, 1.0 h, 1.5 h, 3.0 h) and different nanoparticles formulations (Control group, free $TeTB_2$, $FeTB_2$@INPs, $FeTB_2$@DHA-INPs, and $FeTB_2$@DHA-INPs+NIR) were further investigated, respectively. In addition, the predesigned concentrations of all formulations were 10 μM.

2.7 In Vitro Cytotoxicity

A549 and MCF-7 cells were seeded in 96-well plates (7×10^3 cells well^{-1}) and incubated overnight until fully covered. The cells were then treated with various formulations of nanoparticles at certain concentrations (0.1, 2.5, 5.0, 7.5, 10.0 μg mL^{-1}). After 12 h of incubation, the medium was replaced and the wells were irradiated with a NIR laser (808 nm, 1.5 W cm^{-1}, 3 s well^{-1}) and further incubated for another 12 h. Next, the standard MTT assay was performed to evaluate the inhibition effect of $FeTB_2$@DHA-INPs. Moreover, we take the same approach to evaluate the cytotoxicity of the present nanoparticles on normal cells (RGC-5), and the effect of different DHA concentrations (0.10, 0.75, 1.50, 3.00, 6.00 μg mL^{-1}) on the toxicity of the nanoparticles to MCF-7 cells.

2.8 Cell Apoptosis and Cycle Arrest

To further evaluate the induced apoptosis effect of $FeTB_2$@DHA-INPs on tumor cells, MCF-7 cells were incubated in 6-well plates (5.0×10^5 cells per well) for 24 h until the cells were fully covered. Then the medium were replaced with blank nanoparticles, $FeTB_2$@INPs, and $FeTB_2$@DHA-INPs for 12 h, and then treated with NIR laser for 3 min. After been incubated for another 12 h, the cells were collected (1000 rpm, 5 min, 4 °C) and washed with cold PBS and then suspended in 500 μL binding buffer. Next, 5 μL Annexin V-FITC and 10 μL PI was added to the cell suspension, incubated for 20 min in dark and analyzed by flow cytometry. The concentration of each sample was set as 5 μM.

Next, the cell cycle detection was performed using the same cell processing procedure. Specially, after been incubated with free $FeTB_2$ and $FeTB_2$@DHA-INPs for 48 h, the collected cell suspensions were fixed with 70% ethanol overnight at 4 °C, and further treated with DNA staining for 30 min in the dark. The final cell samples were analyzed with a BD Accuri C6 Flow Cytometer.

2.9 In Vivo Imaging and Biodistribution Analysis

The $FeTB_2$@DHA-INPs solutions containing 45 μg mL^{-1} ICG were intratumorally injected into the nude mice, then in vivo imaging and FL quantitative analysis of ICG (excitation/emission wavelength: 704/735 nm) by the ex/in vivo imaging system (CRI maestro, USA) at 0, 3, 6, 12, and 24 h was performed after injection. In addition, the

mice were sacrificed after 24 h of injection, then the tumor and major organs including the heart, liver, spleen, lung and kidney were collected for imaging and quantitative biodistribution analysis.

2.10 In Vivo Antitumor Efficacy Studies Using a Breast Cancer Model

Male BALB/c mice bearing MCF-7 tumors (~100 mm^3) were randomly divided into five groups (6 per group), and intratumorally administered 150 μL of free $FeTB_2$ or $FeTB_2$@DHA-INPs solution at a concentration of 16.67 mg kg^{-1} (containing 1.64 mg of $FeTB_2$ and 0.11 mg of DHA) and the experimental group was further irradiated with a NIR laser (808 nm, 5 min). Then the mice were treated every 3 days for a total of 5 treatments. The mice were observed for total 24 days and the tumor sizes were measured by an electronic digital caliper every 3 days after treatment and calculated as follows: Tumor volume (V) = $(L \times W^2)/2$, in which the length (L) is the longest part, and the width (W) is the narrowest section perpendicular to the length. After sacrifice, the tumors, livers and kidneys after treatment for 24 days were observed by H&E staining.

2.11 Statistical Analysis Data are expressed as mean ± SD. The differences among groups were determined using one-way ANOVA analysis followed by Tukey's post-test; a P value of < 0.05 was considered significant. Statistical significance was defined as *$P < 0.05$, **$P < 0.01$, ***$P < 0.001$ and n.s. $P > 0.05$, no significance.

3. Results and Discussion

3.1 Synthesis, Assembly and Characterization

In order to effectively increase the efficiency of Fenton reaction, the Fe^{3+}-loaded coordination compound ($FeTB_2$) and the functionalized polymer conjugated with DHA (DHA-$PGlu_{10}$-PEG-DSPE) were designed and synthesized (Figure S1, S2). All the experimental steps were carried out under mild conditions and the yields of obtained products were satisfactory. The chemical structures of the intermediates and final products were confirmed by commonly used spectroscopic techniques including ^1H NMR and ESI-MS, and the results are shown in Figure S3-S5. The assignment of the protons in the molecular structure of the compounds and the molecular weight data were listed in the experimental section. In addition, the molecular weight of functional

polymers was characterized by GPC as shown in Table S1. The results showed that the experimental data were consistent with the standard data of the targeted molecules.

The $FeTB_2$@DHA-INPs were prepared using the classic film hydration method as shown in Scheme 1. In order to maximize the loading capacity of the drugs, different composition proportions of $FeTB_2$, DHA-$PGlu_{10}$-PEG-DSPE, and Lecithin were tested, the results exhibited that the amount of loaded $FeTB_2$ reach 9.86% at the ratio of 5:3:20 (Table S2). In addition, the particle size of this self-assembling formula was acceptable and showed an average particle size of 122.4 nm with polydispersity of 0.212 while those without polymer ligands were about 105.7 nm (Figure 1A). According to the existing reports,[31] this size specification could ensure the particles are not be cleared during blood circulation.

Next, UV-vis spectroscopy was employed to character the drug loaded nanoparticles. The spectrum showed the maximum characteristic absorbance for $FeTB_2$ at 320 nm while DHA did not show obvious absorption (Figure 1B). Moreover, the $FeTB_2$@DHA-INPs showed maximum characteristic absorption peak around 280 nm in the UV spectrum. The morphological characteristics of the prepared $FeTB_2$@DHA-INPs observed by TEM are shown in Figure 1C, and the results showed that the currently nanoparticles process good monodispersity and regular spherical structure. The depolymerized form of nanoparticles after been exposed to NIR light indicated the present nanoparticles showed excellent stimulus-response capacity (Figure 1D). The zeta potential results of the nanoparticles showed that the $FeTB_2$@DHA-INPs was positively charged (23.93 mV) due to conjugated DHA while it was −23.93 mV without conjugation (Figure 1E). When the surface of the positively charged lipid layer is conjugated with the DHA ligands, the surface charge of the nanoparticles could become negative to balance the tension in the aqueous solution to keep monodispersity. Figure 1F showed that different types of nanoparticles present different color states.

3.2 Photothermal Conversion and Stimulus-Response Release

In order to evaluate whether the heat generated by photothermal conversion of the nanoparticles is sufficient to cause the depolymerization of the lipid-polymer shell, the induced heat was recorded and showed in Figure 2A. As exhibited, the control groups

(PBS or hollow nanoparticles) did not show obvious temperature change and the recorded temperature was only about 25 ^{o}C. However, the induced temperature of nanoparticles with ICG encapsulated groups showed the regular of concentration-dependent temperature increase. The induced hyperthermia can increase to about 55 ^{o}C after been exposed to NIR laser for 5 min (20 μg mL^{-1}) and which has exceeded the phase transition temperature of the lipid-polymer shell.[32,33] In addition, the highest induced temperature was about 59 ^{o}C after been exposed to the NIR laser for 5 min and which can even lead to tumor ablation. Figure 2B showed the morphology of the nanoparticles solution by thermal imaging after been irradiated by NIR laser. Thus, based on the NIR irradiation, the present nanoparticles are sufficient to act as a role for controlled drug release or even for photothermal therapy of tumors.

Next, we calculated the amount of the released drug from the nanoparticles under different conditions using the dialysis method. Considering the fact that the lipid-polymer shell of the current nanoparticles can be destroyed by acidic environment, we used three different pH values (7.4, 6.8, or 5.5) to explore the drug release behavior (Figure 2C). Overall, the amounts of released $FeTB_2$ increased more significantly after been exposed to NIR laser as compared with the groups without NIR irradiation. Specially, the amounts of the released $FeTB_2$ increased slowly after been releasing for more than 48 h at pH=7.4. However, the release of $FeTB_2$ was observed with a cumulative drug release of 31.62% after NIR irradiation at pH=7.4 for 48 h. It is worth noting that $FeTB_2$@DHA-INPs released <20% of drug molecules in the absence of NIR irradiation at pH=7.4 and this reduction ratio will become higher in lower pH value. This release behavior indicates that $FeTB_2$@DHA-INPs are highly responsive to NIR light and acidic environment. Figure 2D showed the depolymerization status of the nanoparticles after been released by NIR irradiation at pH=7.4 for 48 h.

3.3 Cellular Uptake and Intracellular ROS Production

The cellular uptake was observed by CLSM and the results are shown in Figure 3A. Only weak red fluorescence intensity (tracing the $FeTB_2$@DHA-INPs) was appeared in A549 cells after been incubated for 1.5 h when compared with it in MCF-7 cells. However, the red fluorescence intensity increased obviously in the cytoplasm

as the incubation time was extended to 3 h in both A549 and MCF-7 cells. Next, we quantified the fluorescence intensity using a flow cytometer (Figure 3B) and further made a comparison (Figure 3C). The quantitative results indicated the amount of accumulated fluorescence intensity in both tumor cells were significant difference after 3 h of incubation (*P<0.05). Thus, the obtained results indicated that the cellular uptake of $FeTB_2$@DHA-INPs present a time-dependent pattern, providing the basis for the study of intracellular ROS levels. Before the ROS evaluation, we use Mito-Tracker Green (MTG) to label mitochondria for the imaging observation. As exhibited in Figure 3D, the obviously strong fluorescence signals were found in both A549 and MCF-7 cells after been incubated for 3 h.

Next, the induced ROS was calculated using the 2', 7'-dichlorodihydrofluorescein diacetate probe (DCFH-DA) and CLSM was used to monitor intracellular ROS production. The free ICG were incubated with MCF-7 cells for 12 h as the control groups. As exhibited in Figure 4A, the amount of ROS generation increased with the concentration of nanoparticles solution. Moreover, the amount of generated ROS in the mitochondria when incubated with $FeTB_2$@DHA-INPs at the concentration of 30 μg mL^{-1} was 7.72-fold than that at 10 μg mL^{-1} (**P<0.01, Figure 4D). Likewise, the production of ROS increased with the increase of incubation time and the amount of generated ROS for 3 h of incubation was much higher than that only incubated for 1 h (***p<0.001, Figure 4B, 4E).

It is important to note that the free ICG also can lead to the increase of intracellular ROS levels. This is because ICG could cause cell apoptosis as a drug molecule and induced ROS generation. In contrast, the $FeTB_2$@DHA-INPs treated group demonstrated much higher levels of ROS generation when compared with free ICG group (Figure 4C, 4F). This may attribute to oxidative stress from the released $FeTB_2$ that is capable of promoting the parent drug release, and ultimately increase in the ROS levels. Moreover, the conjugated DHA further enhanced this generation efficiency. Next, in a parallel experiment we further quantitatively evaluated the ROS levels in A549 cells by flow cytometry after been treated with $FeTB_2$@DHA-INPs (Figure S6). The obtained results showed that the amount of intracellular drugs were about the same

as the results of the fluorescence intensity in MCF-7 cells. Therefore, $FeTB_2$@DHA-INPs exhibited effective antitumor activity in vitro by generating ROS in cancer cells

3.4 Cytotoxicity and Apoptosis Evaluation

Excellent cytotoxicity is the primary characteristic that a new drug molecule is designed to acquire. Thus, the IC_{50} ($mmolL^{-1}$) values in two different tumor cell lines were investigated (Table S3). As expected, the designed $FeTB_2$ showed favored toxicity to selected cell lines after been coordinated with Fe^{3+}. Next, the standard MTT assay was carried out to investigate the in vitro cytotoxicity of $FeTB_2$@DHA-INPs.

As exhibited in Figure 5A and 5B, in general, the cell viability decreased rapidly with increased concentrations of $FeTB_2$@DHA-INPs and which showed superior antitumor properties in both A549 and MCF-7 cells. Compared with the results in A549 cells, free $FeTB_2$ showed much higher cytotoxicity in MCF-7 cells after been incubated for 24 h. However, the free $FeTB_2$ showed lower cytotoxicity at each concentration when compared with $FeTB_2$@DHA-INPs, which attributed to the addition of DHA (Figure 5A, 5B). Undoubtedly, $FeTB_2$@DHA-INPs significantly increased ROS levels through the release of DHA in cancer cells over time. Unlike the chemical drug molecules, $FeTB_2$@DHA-INPs showed much lower cytotoxicity towards the RGC-5 cells as compared with MCF-7 cells (Figure 5C). In addition, the loaded DHA was obviously enhanced the cytotoxicity at each dose concentration (Figure 5D). Thus, the antiproliferative activity of $FeTB_2$@DHA-INPs against RGC-5 is extremely lower may due to the relatively low ROS levels in normal cells. Finally, due to the perfect antitumor performance, $FeTB_2$@DHA-INPs should be considered in the application of cancer therapy for a ROS mediated newly anticancer strategy, together with the enhanced effect of DHA and NIR-response release behavior to minimize the adverse effects of chemotherapy.

The oxidative damage performance of $FeTB_2$@DHA-INPs on MCF-7 cells was further quantified by flow cytometry. As shown in Figure 5E, the MCF-7 cells treated with blank nanoparticles showed much lower apoptotic ratio (11.7%), which indicates the cytotoxicity is mainly caused by the encapsulated $FeTB_2$, while the surface-loaded DHA cannot effectively kill tumor cells as drug molecules. In addition, the apoptosis

rate increased to 23.6% when the cells incubated with $FeTB_2$ loaded nanoparticles ($FeTB_2$@INPs), which is about 13-fold to the control group (2.7%). The apoptosis rate reached to 35.8% when the cells incubated with $FeTB_2$@DHA-INPs for 24 h. As exhibited above, the ROS generated by catalyzing the intracellular hydrogen peroxid through the encapsulated $FeTB_2$, and the surface-loaded DHA further increases ROS levels by supplementing the total peroxide content. Thus, the present nanoparticles demonstrated strong oxidative damage effect on MCF-7 cells and further suggested that the prepared nano-agents showed great potential in cancer therapy.

As shown in Figure 5F and 5G, $FeTB_2$ obviously acts on the G2/M phase of the cell cycle. Specially, the cell percentage in the S phase increases from 37.02% to 42.73%, while which decrease from 57.24% to 34.86% in the G0/G1 phase, this is highly consistent with our previous study that benzothiazole derivatives act as a DNA binding agent to prevent DNA replication.[34] In addition, the results further show that $FeTB_2$@DHA-INPs also interferes with the cell cycle in the G2/M phase. In particularly, the cell percentage in the G0/G1 phase decreased from 57.24% to 44.98% as well. The results indicate that $FeTB_2$ remarkably inhibits DNA replication in the G2/M phase.

Based on the obtained results, the proposed mechanism of $FeTB_2$ molecules on tumor cells is as follows: as $FeTB_2$ is released from $FeTB_2$@DHA-INPs in the tumor cells, it can not only directly kill tumor cells by inhibiting DNA replication, but the coordinated Fe^{3+} is fully released in tumor microenvironment and strongly generated •OH by catalyzes endogenous H_2O_2 to cause oxidative damage. Thus it shows the favorable synergistic effect from the $FeTB_2$ molecules and provides a ROS-mediated high efficiency antitumor strategy.

3.5 In Vivo Imaging Study

In order to observe the delivery of $FeTB_2$@DHA-INPs in vivo, ICG loaded $FeTB_2$@DHA-INPs were injected intratumorally into BALB/c mice bearing MCF-7 tumors (n=3). As shown in Figure 6A, in the initial 3 h after injection, the nanoparticles did not spread obviously and were mainly accumulated in the tumor site. However, the nanoparticles were gradually spread to the whole body along with blood circulation and the fluorescence signals were significant in the organs (such as liver and kidneys) at 12

h post-injection. It is worth mentioning that the fluorescence signals in tumor sites still at high levels at 24 h post-injection. Therefore, the obtained results exhibited excellent endocytosis and accumulation performance of $FeTB_2$@DHA-INPs in tumor sites with the effect of the lipid-polymer shells.

Next, we deeply evaluated the fluorescence signals intensity accumulated in tumor and various organs after 24 h of post-injection, and the results exhibited that significant fluorescence signals were accumulated in the organs (Figure 6B). These results of ICG imaging in vivo further exhibited that the small therapeutic molecules can be effectively prevented from being cleared by the lipid–polymer structure in the living body.

3.6 In Vivo Antitumor Therapy

We further applied the $FeTB_2$@DHA-INPs to BALB/c mice to evaluate the antitumor effect in vivo. As shown in Figure 6C, different from other experimental groups, the tumor volumes in the control group increased by approximately 3.3-fold in 6 days, while the experimental groups showed a moderate increase due to the obvious antineoplastic efficacy. In addition, during the period of 24 days treatment, the tumor volumes in group **b**, **c**, **d** increased by approximately 20.0-fold, 16.8-fold, and 12.6-fold respectively, while the $FeTB_2$@DHA-INPs added NIR irradiation group (group **e**) showed an insignificant tumor volume increase (only 5.0-fold).

Moreover, the body weight in the experimental group (group **e**) increased slightly while it in group **d** showed much higher level, indicating that the antitumor efficiency of therapeutic agents was affected by the NIR mediated drug release (Figure 6D). Specially, the experimental group showed an amazing performance of tumor ablation and the tumor inhibition reached by 81.4% after 24 days of post-injection (Figure 6E, 6F). The results of gross examination and weights of the mice also showed that $FeTB_2$@DHA-INPs significantly inhibited tumor growth compared to other treatment groups (***$p < 0.001$, Figure 6C, 6D).In addition, when compared with group **c**, the results in group **b** (Free $FeTB_2$) showed relatively slighter tumor weight change during the 24 days of treated period, indicating the prepared nanosystems can effectively prevent drug molecules from being removed (Figure 6C, 6D).

Next, the H&E staining was carried out to evaluate the ROS mediated antitumor

effect and potential toxicity of $FeTB_2$@DHA-INPs. As shown in Figure 6G, the results of group **e** exhibited more effective antitumor effects and clearly showed tumor necrosis, and destroy of blood vessels. The toxic side effects of prepared nanoparticles should not be negligible, however, the toxicity of $FeTB_2$@DHA-INPs in the major organs in all experimental groups showed no significant organ damage or inflammation lesion, which attributed to ROS mediated oxidative damage. These satisfactory results fully demonstrated the excellent biocompatibility of $FeTB_2$@DHA-INPs and showed great potential as a nanotheranostic agent for ROS mediated anticancer therapy.

4. Conclusion

In summary, we successfully developed a multifunctional $FeTB_2$-engineered and DHA-grafted nanodrug agent, to construct an innovative ROS-killing nano-delivery system ($FeTB_2$@DHA-INPs). The encapsulated ICG enables the nanosystems to have NIR-responsive drug release. The released $FeTB_2$ could not only directly kill tumor cells by inducing DNA arrest, but the Fe^{3+} catalyzes the Fenton reaction to increase ROS levels, which further leads to oxidative damage. Moreover, the surface-loaded DHA further complements the intracellular H_2O_2 and effectively enhances ROS yields. When compared with free $FeTB_2$, $FeTB_2$@DHA-INPs exhibited much lower cytotoxic in normal cells and superior antitumor activity at the same dose of $FeTB_2$. Moreover, the polymer chains design enables the nanosystem prolonged circulation in the blood and effective accumulation in tumor cells. These results provide an alternative strategy to antitumor with ROS mediated oxidative damage, which showed great potential in clinical application.

Supporting Information

Synthesis procedures and other supplementary data.

Statement

All animal experiments were complied with the Regulations on the Administration of Laboratory Animals and the relevant national laws and regulations, and performed under the guidance approved by the Laboratory Animal Ethics Committee at School of Medicine, Southeast University (Nanjing, China).

Acknowledgements

We are highly grateful to the financial support from the National Natural Science Foundation of China (Grant Nos. 21905138 and 21628101), the National Natural Science Foundation of Jiangsu Province (Grant Nos. BK20190756), the project funded by China Postdoctoral Science Foundation (No. 2019M651841), the National Key Research and Development Program of China (2016YFD0600801), the Top-notch Academic Programs Project of Jiangsu Higher Education Institutions (TAPP, Grant Nos. PPZY2015C221) and Priority Academic Program Development of Jiangsu Higher Education Institutions (PAPD).

References

(1) Dolmans, D.; Fukumura, D.; Jain, R. K. Photodynamic Therapy for Cancer. *Nat. Rev. Cancer* **2003**, 3, 380-387.

(2) Agostinis, P.; Berg, K.; Cengel, K. A.; Foster, T. H.; Girotti, A. W.; Golab, J. Photodynamic Therapy of Cancer: An Update. *Ca-Cancer J. Clin.* **2011**, 61, 250-281.

(3) Kim, S. U.; Park, Y. H.; Min, J. S.; Sun, H. N.; Han, Y. H.; Hua, J. M.; Lee, T. H.; Lee, S. R.; Chang, K. T.; Kang, S. W.; Kim, J. M.; Yu, D. Y.; Lee S. H.; Lee, D. S. Peroxiredoxin I is A ROS/p38 MAPK-Dependent Inducible Antioxidant that Regulates NF-κB-Mediated iNOS Induction and Microglial Activation *J. Neuroimmunol* **2013**, 259, 26-36.

(4) Park, Y. H.; Kim, S. U.; Lee, B. K.; Kim, H. S.; Song, I. S.; Shin, H. J.; Han, Y. H.; Chang, K. T.; Kim, J. M.; Lee, D. S.; Kim, Y. H.; Choi, C. M.; Kim, B. Y.; Yu, D. Y. Prx I Suppresses K-ras-Driven Lung Tumorigenesis by Opposing Redox-Sensitive ERK/Cyclin D1 Pathway. *Antioxid. Redox Sig.* **2013**, 19, 482-496.

(5) Murphy, M. P.; Holmgren, A.; Larsson, N. G.; Halliwell, B.; Chang, C. J.; Kalyanaraman, B.; Rhee, S. G.; Thornalley, P. J.; Partridge, L.; Gems, D.; Nystrom, T.; Belousov, V.; Schumacker, P. T.; Winterbour, C. C. Unraveling the Biological Roles of Reactive Oxygen Species. *Cell Metab.* **2011**, 13, 361-366.

(6) Dixon, S. J.; Lemberg, K. M.; Lamprecht, M. R.; Skouta, R.; Zaitsev, E. M.; Gleason, C. E.; Patel, D. N.; Bauer, A. J.; Cantley, A. M.; Yang, W. S.; Morrison III, B.; Stockwell, B. R. Ferroptosis: An Iron-Dependent Form of Nonapoptotic Cell Death. *Cell* **2012**, 149, 1060-1072.

(7) Shi, L. L.; Guan, Q. H.; Gao, X. H.; Jin, X.; Xu, L.; Shen, J.; Wu, C. W.; Zhu, X. Y.; Zhang, C. Reaction-based color-convertible fluorescent probe for ferroptosis identification. *Anal. Chem.* **2018**, 90, 9218−9225.

(8) Zhu, T.; Shi, L. L.; Yu, C. Y.; Dong, Y. B.; Qiu, F.; Shen, L. Y.; Qian, Q. H.; Zhou, G. Y.; Zhu, X. Y. Ferroptosis promotes photodynamic therapy: supramolecular photosensitizer-inducer nanodrug for enhanced cancer treatment. *Theranostics* **2019**, 9, 3293-3307.

(9) Zhou, Z.; Song, J.; Tian, R.; Yang, Z.; Yu, G. C.; Lin, L. S.; Zhang, G. F.; Fan, W. P.; Zhang, F. W.; Niu, G.; Nie, L. M.; Chen, X. Y. Activatable Singlet Oxygen Generation from Lipid Hydroperoxide Nanoparticles for Cancer Therapy. *Angew. Chem. Int. Edit.* **2017**, 129, 6492-6496.

(10) Hu, P.; Wu, T.; Fan, W. P.; Chen, L.; Liu, Y. Y.; Ni, D. L.; Bu, W. B.; Shi, J. L. Near Infrared-assisted Fenton Reaction for Tumor-Specific and Mitochondrial DNA-targeted Photochemotherapy. *Biomaterials* **2017**, 141, 86-95.

(11) Tang, Z. M.; Zhang, H. L.; Liu, Y. Y.; Ni, D. L.; Zhang, H.; Zhang, J. W.; Yao, Z. W.; He, M. Y.; Shi, J. L.; Bu, W. B. Antiferromagnetic Pyrite as the Tumor Microenvironment-Mediated Nanoplatform for Self-Enhanced Tumor Imaging and Therapy. *Adv. Mater.* **2017**, 29, 1701683.

(12) Ahmed, K.; Yellamelli, V. V. S.; Mohammed, N. A.; Sultana, F.; Methuku, K. R. Recent Advances on Structural Modifications of Benzothiazoles and Their Conjugate Systems as Potential Chemotherapeutics. *Expert Opin Investig Drugs* **2012**, 21, 619-635.

(13) Dubey, R.; Shrivastava, P. K.; Basniwal, P. K.; Bhattacharya, S.; Moorthy, N. S. 2-(4-Aminophenyl) Benzothiazole: A Potent and Selective Pharmacophore with Novel Mechanistic Action towards Various Tumour Cell Lines. *Mini-Rev Med Chem* **2006**, 6, 633-637.

(14) Noolvi, M. N.; Patel, H. M.; Kaur, M. Benzothiazoles: Search for Anticancer Agents. *Eur J Med Chem* 2012, 54, 447-462.

(15) Sleebs, B. E.; Kersten, W. J.; Kulasegaram, S.; Nikolakopoulos, G.; Hatzis, E.; Moss, R. M.; Parisot, J. P.; Yang, H.; Czabotar, P. E.; Fairlie, W. D.; Lee, E. F.; Adams, J. M.; Chen, L.; Delft, M. F. V.; Lowes, K. N.; Wei, A.; Huang, D. C.; Colman, P. M.; Street, I. P.; Baell, J. B.; Watson, K.; Lessene, G. Discovery of Potent and Selective Benzothiazole Hydrazone Inhibitors of BCL-XL. *J Med Chem* **2013**, 56, 5514-5540.

(16) Lessene, G.; Czabotar, P. E.; Sleebs, B. E.; Zobel, K.; Lowes, K. N.; Adams, J. M.; Baell, J. B.; Colman, P. M.; Deshayes, K.; Fairbrother, W. J.; Flygare, J. A.; Gibbons, P.; Kersten, W. J.;

Kulasegaram, S.; Moss, R. M.; Parisot, J. P.; Smith, B. J.; Street, I. P.; Yang, H.; Huang, D. C.; Watson, K. G. Structure-Guided Design of A Selective BCL-XL Inhibitor. *Nat Chem Biol* **2013**, 9, 390-397.

(17) Racane, L.; Pavelic, S. K.; Nhili, R.; Depauw, S.; Paul-Constant, C.; Ratkaj, I.; David-Cordonnier, M. H.; Pavelic, K.; Tralic-Kulenovic, V.; Karminski-Zamola, G. New Anticancer Active and Selective Phenylene-Bisbenzothiazoles: Synthesis, Antiproliferative Evaluation and DNA binding. *Eur J Med Chem* **2013**, 63, 882-891.

(18) Hussein, B. H.; Azab, H. A.; El-Azab, M. F.; El-Falouji, A. I. A Novel Anti-tumor Agent, Ln (Ⅲ) 2-Thioacetate Benzothiazole Induces Anti-angiogenic Effect and Cell Death in Cancer Cell Lines. *Eur J Med Chem* **2012**, 51, 99-109.

(19) Singh, N. P.; Lai, H. Selective Toxicity of Dihydroartemisinin and Holotransferrin toward Human Breast Cancer Cells. *Life Sciences* **2001**, 70, 49-56.

(20) Kang, M. H.; Reynolds, C. P. Bcl-2 Inhibitors: Targeting Mitochondrial Apoptotic Pathways in Cancer Therapy. *Clin Cancer Res* **2009**, 15, 1126-1132.

(21) Nariculam, J.; Freeman, A.; Bott, S.; Munson, P.; Cable, N.; Brookman-Amissah, N.; Williamson, M.; Kirby, R. S.; Masters, J.; Feneley, M. Utility of Tissue Microarrays for Profiing Prognostic Biomarkers in Clinically Localized Prostate Cancer: the Expression of BCL-2, E-cadherin, Ki-67 and p53 as Predictors of Biochemical Failure after Radical Prostatectomy with Nested Control for Clinical and Pathological Risk Factors. *Asian J Androl* **2009**, 11, 109-118.

(22) Zhang, X. Y.; Guo, Z. Q.; Ji, S. Q.; Zhang, M.; Jiang, N.; Li, X. S.; Zhou, L. Q. Small Interfering RNA Targeting HMGN5 Induces Apoptosis via Modulation of A Mitochondrial Pathway and BCL-2 Family Proteins in Prostate Cancer Cells. *Asian J Androl* **2012**, 14, 487-492.

(23) Hussein, B. H.M.; Azab, H. A.; El-Azab, M. F.; El-Falouji, A. I. A novel anti-tumor agent, Ln(III) 2-thioacetate benzothiazole induces anti-angiogenic effect and cell death in cancer cell lines. *Eur J Med Chem* **2012**, 51, 99-109.

(24) Gao, Z. G., Li, Y. J.; You, C. Q.; Sun, K.; An, P. J.; Sun, C.; Wang, M. X.; Zhu, X. L.; Sun, B. W. Iron Oxide Nanocarrier-Mediated Combination Therapy of Cisplatin and Artemisinin for Combating Drug Resistance Through Highly Increased Toxic Reactive Oxygen Species Generation. *ACS Appl. Bio Mater.* **2018**, 1, 270-280.

(25) You, C. Q.; Wu, H. S.; Wang, M. X.; Zhang, Y. W.; Wang, J. W.; Luo, Y. H.; Zhai, L. H.; Sun, B. W.; Zhang, X. Y.; Zhu, J. Near-Infrared Light and pH Dual-Responsive Targeted Drug Carrier

Based on Core-CrosslinkedPolyaniline Nanoparticles for Intracellular Delivery of Cisplatin. *Chem. Eur. J.* **2017**, 23, 5352-5360.

(26) Tang, G. S.; Xiong, R. H.; Lv, D.; Xu, R. X.; Braeckmans, K.; Huang, C. B.; De Smedt, S. C. Gas-Shearing Fabrication of Multicompartmental Microspheres: A One-Step and Oil-Free Approach. *Advanced Science* **2019**, 6, 1802342-1802351.

(27) Hua, D. W.; Liu, Z. C.; Wang, F.; Gao, B. H.; Chen, F.; Zhang, Q. L.; Xiong, R. H.; Han, J. Q.; Samal, S. K.; De Smedt, S. C.; Huang, C. B. PH Responsive Polyurethane (core) and Cellulose Acetate Phthalate(shell) Electrospun Fibers for Intravaginal Drug Delivery. *Carbohydrate Polymers* **2016**, 151, 1240–1244

(28) You, C. Q.; Gao, Z. G.; Wu, H. S.; Sun, K.; Ning, L. K.; Lin, F.; Sun, B. W.; Wang, F. Reactive Oxygen Species Mediated Theranostics Using A Fenton Reaction Activable Lipopolymersome. *J. Mater. Chem. B* **2019**, 7, 314-323.

(29) Jing, X. N.; Zhi, Z.; Jin, L. M.; Wang, F.; Wu, Y. S.; Wang, D. Q.; Yan, K.; Shao, Y. Q.; Meng, L. J. PH/Redox Dual-Stimuli-Responsive Cross-linked Polyphosphazene Nanoparticles for Multimodal Imaging-Guided Chemo-Photodynamic Therapy. *Nanoscale* **2019**, 11, 9457-9467.

(30) Gao, S. T.; Tang, G. S.; Hua, D. W.; Xiong, R. H.; Han, J. Q.; Jiang, S. H.; Zhang, Q. L.; Huang, C. B. Stimuli-responsive bio-based polymeric systems and their applications. *Journal of Materials Chemistry B* **2019**, 7, 709–729.

(31) You, C. Q.; Wu, H. S.; Gao, Z. G.; Sun, K.; Chen, F. H.; Tao, W. A.; Sun, B. W. Subcellular Co-delivery of Two Different Site-Oriented Payloads Based on Multistage Targeted Polymeric Nanoparticles for Enhanced Cancer Therapy. *J. Mater. Chem. B* **2018**, 6, 6752-6766.

(32) You, C. Q.; Wang, M. X.; Wu, H. S.; An, P. J.; Pan, M. M.; Luo, Y. H.; Sun, B. W. Near Infrared Radiated Stimulus-Responsive Liposomes Based on Photothermal Conversion as Drug Carriers for Co-delivery of CJM126 and Cisplatin. *Materials Science and Engineering C* **2017**, 80, 362-370.

(33) Liu, Z. J.; Le, Z. C.; Lu, L. J.; Zhu, Y.; Yang, C. B.; Zhao, P. F.; Wang, Z. Y.; Shen, J.; Liu, L. X.; Chen, Y. M. Scalable Fabrication of Metal-Phenolic Nanoparticles by Coordination-Driven Flash Nanocomplexation for Cancer Theranostics. *Nanoscale* **2019**, 11, 9410-9421.

(34) You, C. Q.; Yu, J.; Sun, Y.; Luo, Y. H.; Zhang, X. Y.; Zhu, J.; Sun, B. W. Enhanced Cytotoxicity by A Benzothiazole-containing Cisplatin Derivative in Breast Cancer Cells. *New J. Chem.* **2017**, 41, 773-785.

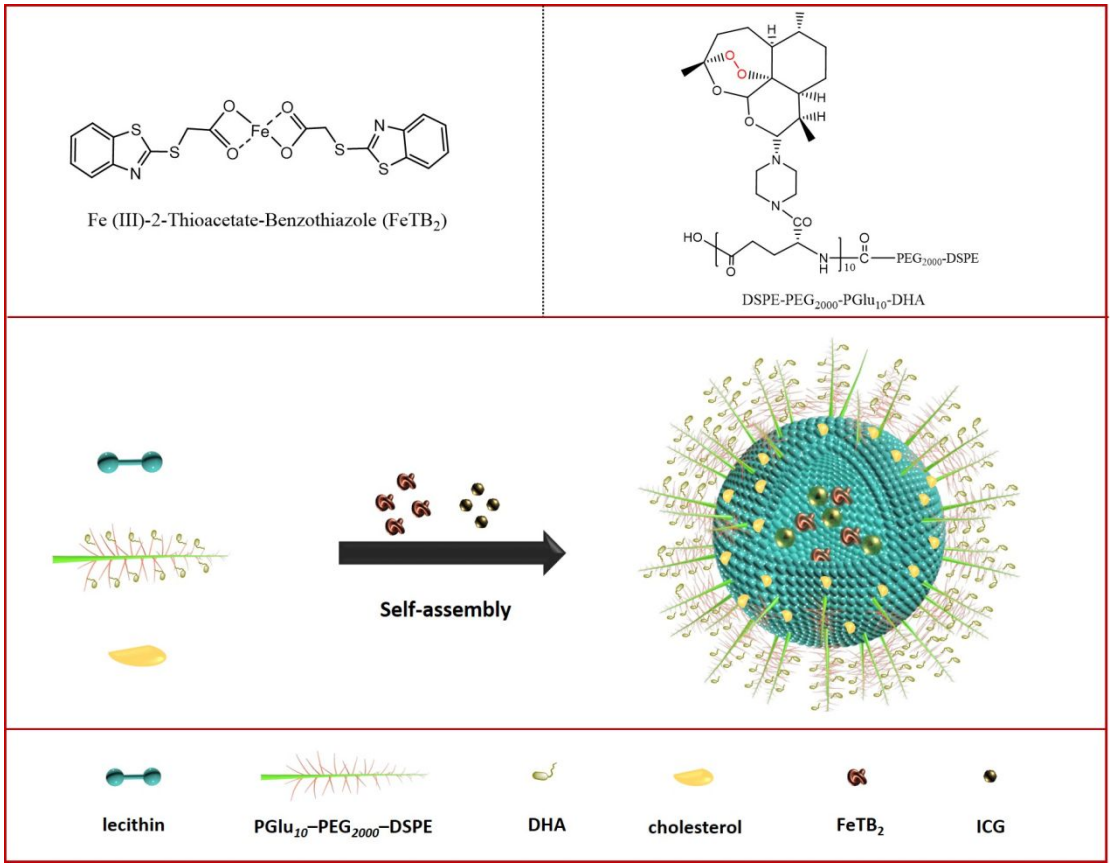

Scheme 1 Self-assembly of ICG and $FeTB_2$-embedded DHA-grafted nanoparticles ($FeTB_2$@DHA-INPs).

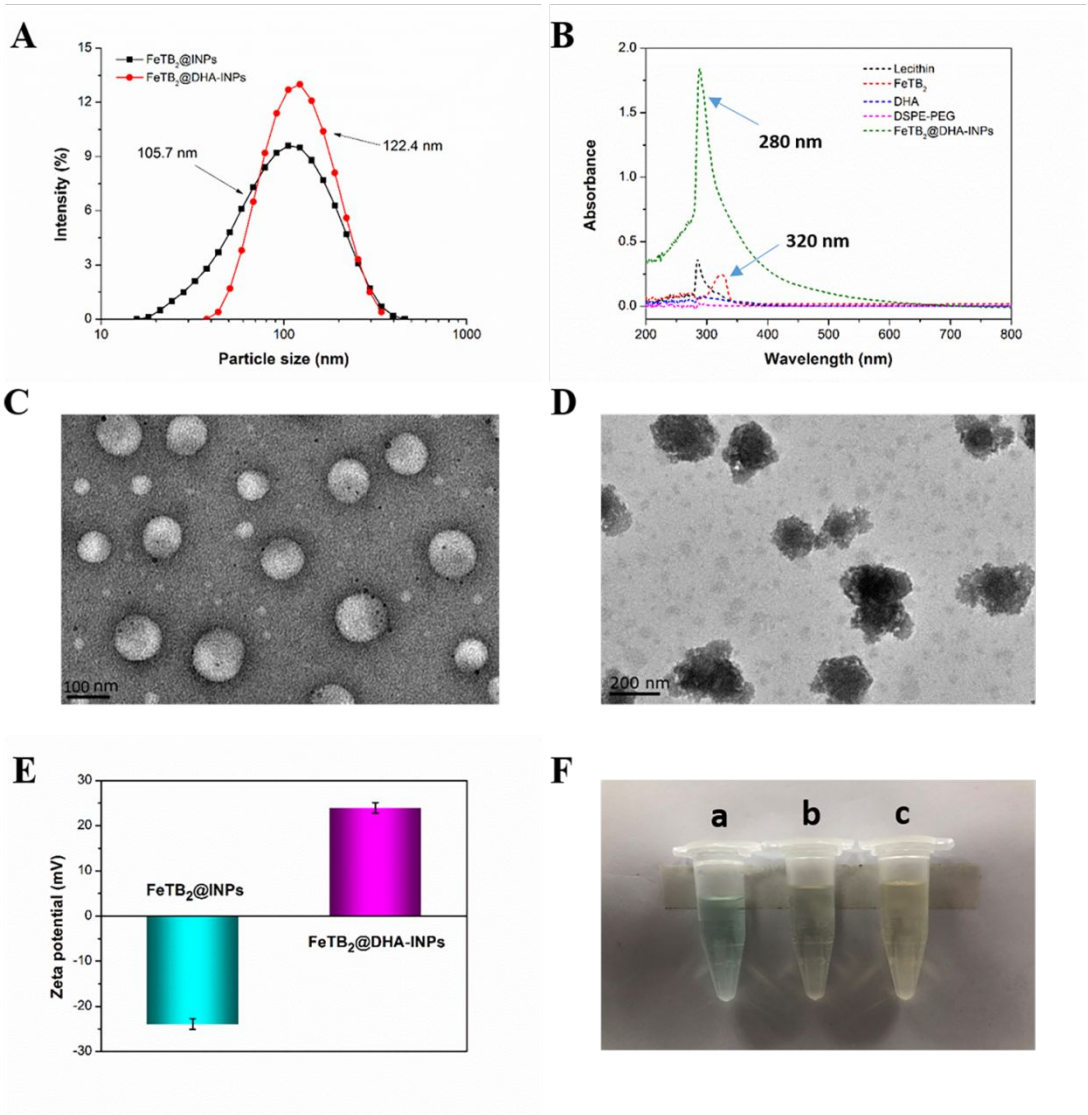

Figure 1 **A**, Size distribution of $FeTB_2$@INPs and $FeTB_2$@DHA-INPs determined by DLS. **B**, UV−vis −NIR spectra of $FeTB_2$ in methanol, Lecithin, DHA, DSPE-PEG_{2000} and $FeTB_2$@DHA-INPs suspensions in phosphate buffer (pH = 7.4). **C**, TEM image of $FeTB_2$@DHA-INPs. Scale bar: 100 nm. **D**, TEM image of $FeTB_2$@DHA-INPs in PBS (pH = 7.4) after 5 min post-irradiation. Scale bar: 200 nm. **E**, The Zeta potential on the surface of $FeTB_2$@INPs and $FeTB_2$@DHA-INPs. **F**, Images of nanoparticles suspension at 25 °C (pH = 7.4): a, DHA-INPs; b, $FeTB_2$@DHA-INPs; c, $FeTB_2$@DHA-INPs+NIR.

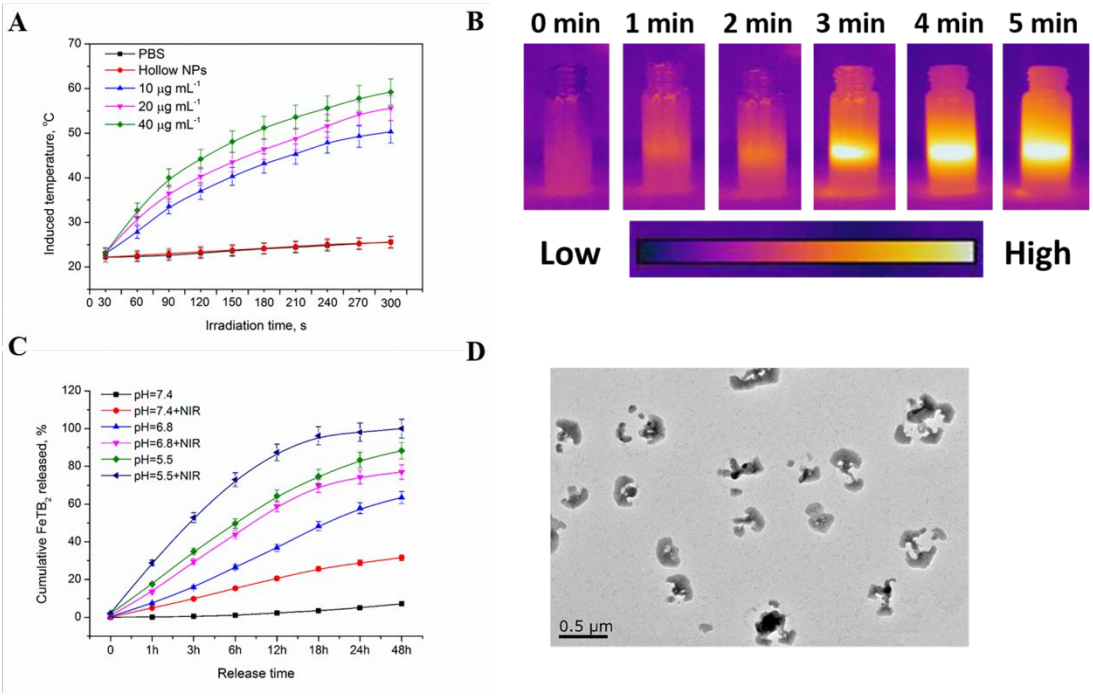

Figure 2 **A**, The NIR induced temperature curves of nanoparticles suspension with different concentrations (10, 20, 40 μg mL^{-1}). **B**, The pictures of $FeTB_2$@DHA-INPs suspension at different time points (0, 1, 2, 3, 4, 5 min) imaged by infrared (IR) thermal camera. **C**, NIR dependent release of $FeTB_2$ from the $FeTB_2$@DHA-INPs at different pH (7.4, 6.8, 5.5). **D**, TEM image of $FeTB_2$@DHA-INPs in PBS (pH=7.4) after 48 h post-irradiation.

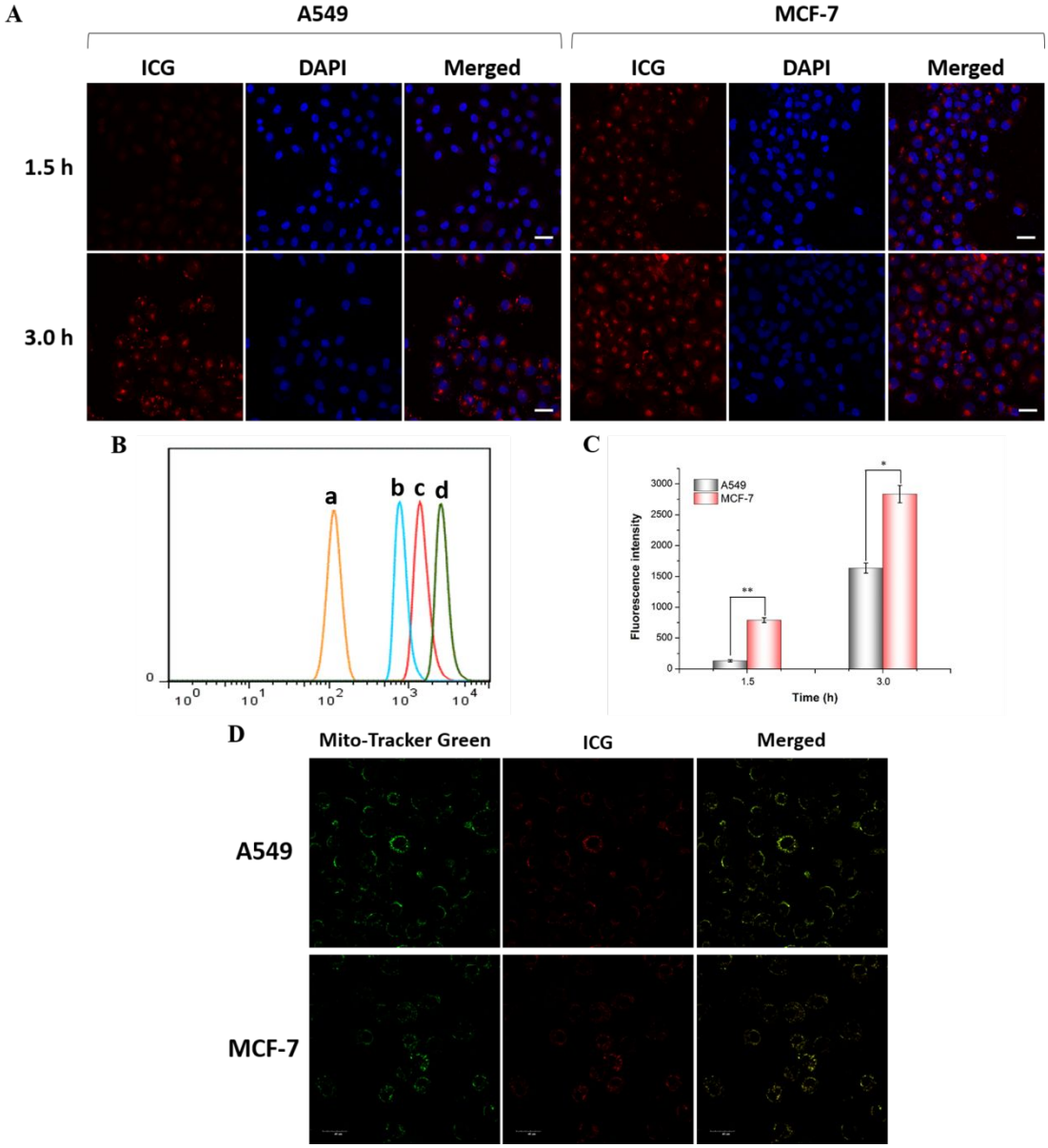

Figure 3 A, CLSM images of A549 and MCF-7 cells incubated with $FeTB_2$@DHA-INPs for different period of time at an equivalent ICG concentration of 50 μg mL^{-1} (Scale bar, 20 μm). Flow cytometric analysis (**B**) and quantitation (**C**) of the ICG fluorescence intensity in A549 and MCF-7 cells (A549: a, 0.5 h, c, 3.0 h; MCF-7: b, 0.5 h, d, 3.0 h). **D**, Internalization of $FeTB_2$@DHA-INPs suspension (equivalent to 50 μg mL^{-1} ICG) by MCF-7 cells for 3 h, analyzed by CLSM (Scale bar, 40 μm).

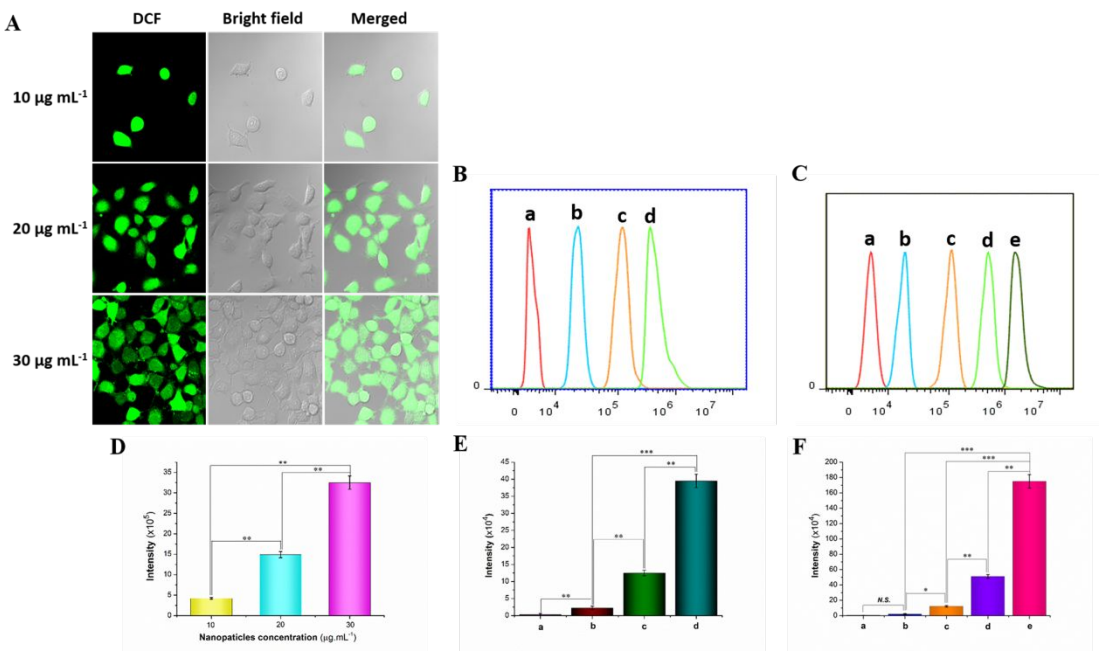

Figure 4 Evaluation the capability of ROS generation of $FeTB_2$@DHA-INPs in vitro. **A**, CLSM images of MCF-7 cells incubated with $FeTB_2$@DHA-INPs for different concentrations (10, 20, 30 μg mL^{-1}) and quantitated analysis (**D**). **B**, Flow cytometric analysis of ROS levels in MCF-7 cells with different incubation time (a, 0.5 h; b, 1.0 h; c, 1.5 h; d, 3.0 h) and quantitated analysis (**E**). **C**, Flow cytometric analysis of ROS levels in MCF-7 cells with different nanoparticle formations (a, Control group; b, Free $FeTB_2$; c, $FeTB_2$@INPs; d, $FeTB_2$@DHA-INPs; e, $FeTB_2$@DHA-INPs+NIR) and quantitated analysis (**F**). (n = 3), *: $P < 0.05$, **: $P < 0.01$ and ***: $P < 0.001$.

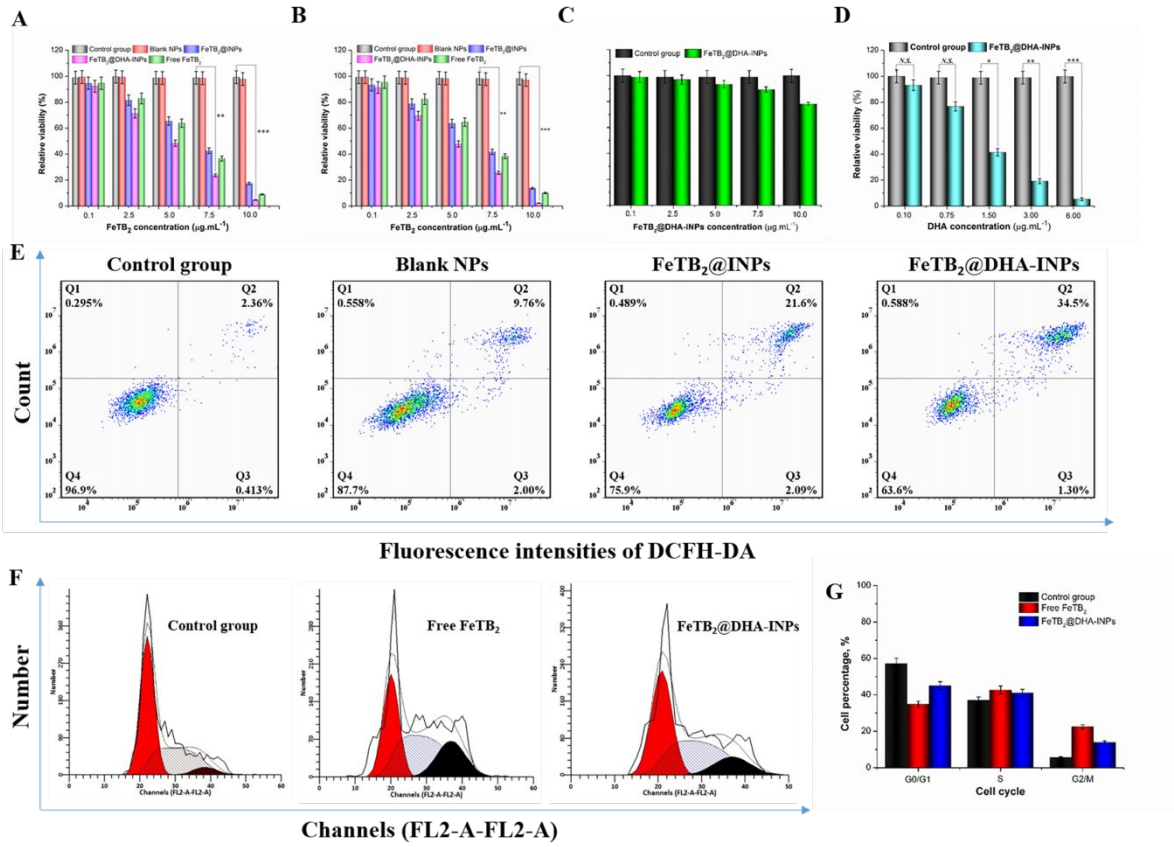

Figure 5 Quantitative evaluation of cell viability for A549 cells (**A**) and MCF-7 cells (**B**) treated with different nanoparticle formulations for 24 h. **C**, Quantitative evaluation of cell viability for RGC-5 cells treated with $FeTB_2$@DHA-INPs. **D**, Quantitative evaluation of cell viability for MCF-7 cells treated with NPs for different DHA concentrations. **E**, The apoptosis of MCF-7 cells treated with $FeTB_2$@DHA-INPs. (n = 3). **F**, Effect of $FeTB_2$ and $FeTB_2$@DHA-INPs on cell cycle arrest in MCF-7 cells and quantitative analysis (**G**). *N.S.*: $P > 0.05$, no significance, *: $P < 0.05$, **: $P < 0.01$, ***: $P < 0.001$.

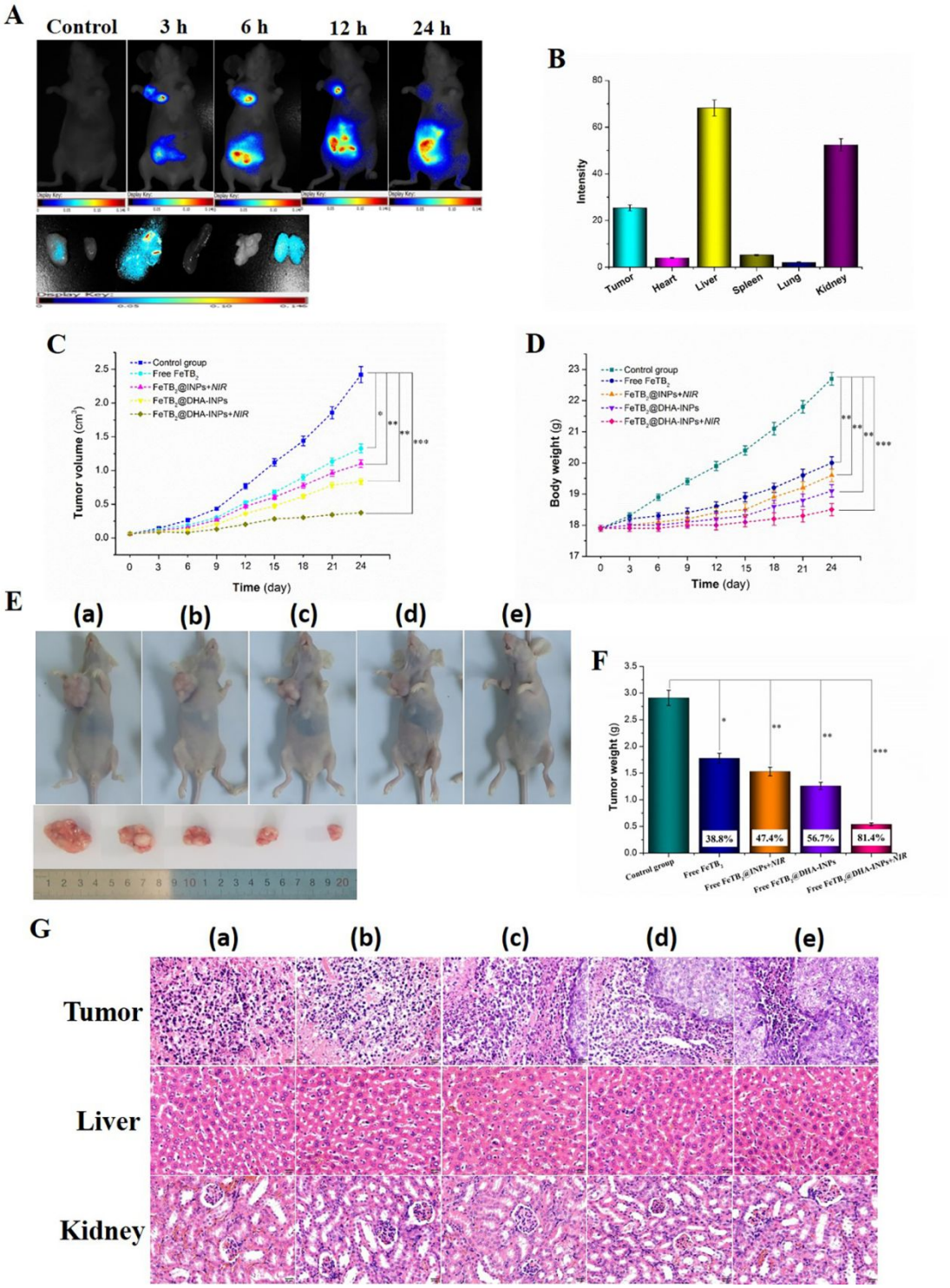

Figure 6 A, In vivo fluorescence imaging of MCF-7 breast tumor-bearing nude mice and major organs of mice sacrificed 24 h after intratumoral injection of $FeTB_2$@DHA-INPs. **B**, Quantitative evaluation of fluorescence intensity of tumor and major organs of mice sacrificed 24 h after intratumoral injection. **C**, Relative tumor volume growth curves in different treatment groups of tumor-bearing mice (were normalized to their initial sizes). **D**, Mice weight growth curves in different treatment groups of tumor-bearing mice. **E**, Representative photographs of mice bearing

MCF-7 breast tumors treated with different NPs suspensions: (a), control group; (b), Free $FeTB_2$; (c), $FeTB_2$@INPs+NIR; (d), $FeTB_2$@DHA-INPs; (e), $FeTB_2$@DHA-INPs+NIR. **F**, The tumor weight in different groups of tumor-bearing mice after incubation for 24 days. **G**, H&E stained images of tumors and major organs from mice sacrificed after incubation for 24 days. Error bars represent the standard deviation of six mice per group. Data are presented as the mean ± SD (n = 6, *$p < 0.05$, **$p < 0.01$, ***$p < 0.001$. vs. control group).